analytical chemistry

pubs.acs.org/ac Article

Numerical Modeling for Sensitive and Rapid Molecular Detection by Membrane-Based Immunosensors

Hiroto Okuyama, Takanori Tamaki, Yuhei Oshiba, Hiroshi Ueda, and Takeo Yamaguchi*

Cite This: *Anal. Chem.* 2021, 93, 7210−7219 Read Online

ACCESS | Metrics & More | Article Recommendations | Supporting Information

ABSTRACT: Rapid, simple, and sensitive point-of-care testing (POCT) has attracted attention in recent years due to its excellent potential for early disease diagnosis and health monitoring. The flow-through biosensor design is a candidate for POCT that utilizes the small-sized pores of a porous membrane as a recognition space where it emits a signal comparable to that of a conventional enzyme-linked immunosorbent assay within 35 min of detection time. In this paper, we present a numerical model for this immunosensing technology to systematically design an improved recognition system. The model considers mass transfer into the pore (convection and diffusion), the kinetics between the immobilized receptor and the target molecule, and the flow conditions, successfully leading to a bottleneck step (capture of secondary antibody) in sandwich-type detection. Our simulation results also show that this problem can be solved by adopting both appropriate receptors and analytical conditions. Eventually, the requirements to achieve the sensitivity required for POCT were fulfilled, which will allow for further development of immunosensing devices for disease detection.

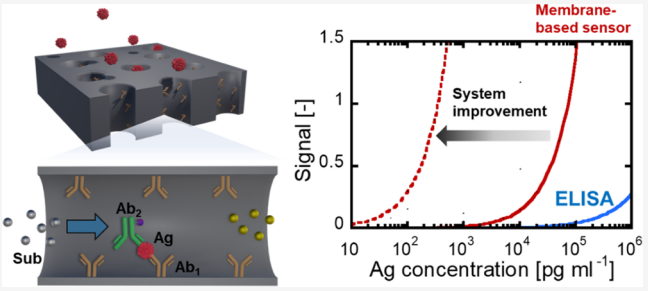

Biosensors are chemical sensors that use biological molecular-recognition mechanisms such as enzymatic reactions and antigen−antibody systems.[1] They can be applied in medical diagnostics by targeting trace amounts of biomarkers that are present in biological samples. Point-of-care testing (POCT) that can be conducted at home or bedside has become an important research focus in recent years. In the development of biosensor diagnostic technologies, various biomarkers, including prostate-specific antigens,[2,3] C-reactive proteins,[4] cardiac troponin[5] (markers of acute myocardial infarction), and cytokines[6] (inflammatory markers), have been investigated.

While the discovery of functional biomarkers and their receptors for disease detection is critical,[7−10] a practicable detection system design is also essential for biosensor development. The lateral flow assay is a rapid and easy-to-use detection method that is now widely used in clinical practice; however, its low sensitivity is a limitation.[11] Thus, sensitive sensing techniques, including immune-polymerase chain reaction,[12] have been developed to enable extremely high sensitivity and specificity. However, sensitive sensing systems have limitations such as the expensive equipment required and long detection times. Enzyme-linked immunosorbent assay (ELISA)[13] is the most common technique used for lab-scale diagnostic applications and is expected to be a fundamental technology in POCT design. Although ELISA is highly sensitive compared with other methods that employ an antigen−antibody system, this method is still time-consuming and labor-intensive[14] because of its rate-limiting step during the diffusion of substances to the reaction site inside the well.[15] Hence, a novel rapid and simple detection system with high sensitivity is required for POCT.

Recently, we succeeded in developing a membrane-based immunosensor that is rapid and sensitive (Figure 1a).[16] This sensor is based on a porous track-etched membrane, and nanometer- to micrometer-sized cylindrical pores are used as molecular-recognition channels. To achieve a high-reactivity space, the captured antibodies were uniformly and densely immobilized within the small-sized pores using a combination of the plasma-induced graft polymerization technique[17−19] and the active ester method. In addition to this reactive pore structure, we also eliminated the diffusional rate-limiting effect with an active solution (analyte) flow into the pores.[20] As a result, the time required for the sandwich-type detection test was reduced to ∼35 min from the 2 h required by ELISA. Moreover, this membrane-based sensor showed comparable signal strength to ELISA despite the contaminants. Although there are some reports regarding sensors that use a membrane as a substrate,[3,21,22] our system was superior in terms of sensitivity, rapidity, and amount of sample employed. The

Received: January 19, 2021
Accepted: March 18, 2021
Published: May 6, 2021

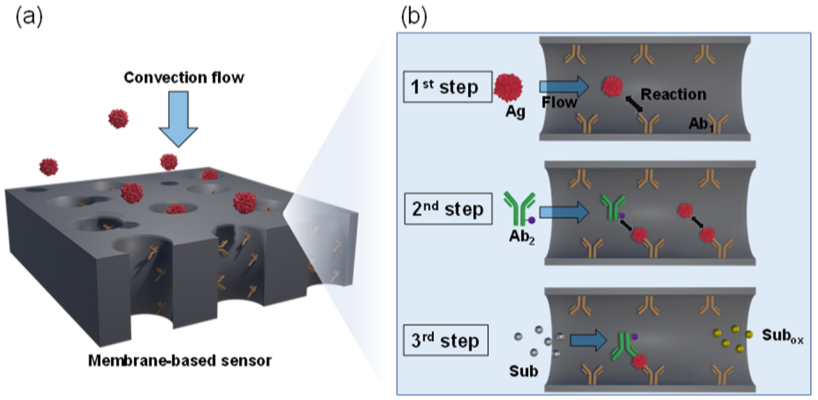

Figure 1. (a) Schematic illustration of a membrane-based biosensor using solution flow (convection flow). (b) Numerical model considering mass transfer via flow and associated molecular-recognition reaction. There are three steps for sandwich-type detection: flow of the (1) antigen (Ag), (2) detection antibody (Ab_2), and (3) corresponding substrate (Sub).

Table 1. Sensor Types and Their Performances

	Reaction space	Specific surface area	Reaction system	Detection time	Potential performance
ELISA	well surface (radius ~ 3 mm)	low	diffusion	>2 hrs	medium
Lateral flow assay	test line (~1.5mm × 4mm)		flow	~30 min	low
Microfluidic sensor	microchannel (radius ~ 1 mm)		flow	~30 min	high
Membrane-based sensor	membrane pore channel (radius ~1 μm)	high	flow	~30 min	very high

small pores (~1 μm) can provide a high surface area, which leads to high reactivity. Thus, the sensor is also proposed to be a superior candidate for POCT than microfluidic biosensors[23−25] that use micrometer- to millimeter-sized channels (comparison of the sensors is shown in Table 1).

Meanwhile, the limit of detection (LOD) of our system is currently ~1 ng/mL. Since the required LOD for detecting a wide variety of biomarkers is ~10−100 pg/mL, the test conditions and system itself need to be improved. The membrane-based system has several recognition steps and parameters (e.g., flow rate of the analyte and detection reagents, reaction time, receptor density in the pore, and membrane thickness) that can affect its sensitivity; thus, it will be time-consuming to experimentally investigate appropriate conditions. In such cases, a comprehensive study using the numerical model is useful.

Models for the adsorption/recognition behavior of target molecules have been studied using various biosensors, including ELISA,[26] surface plasmon resonance,[27] microfluidic devices,[28,29] and magnetic biosensors.[30] Vijayendran et al. have developed a transport-kinetic model for diffusion-based molecular recognition.[31] Alam et al. presented a mathematical model for the adsorption/extraction of analytes on a solid surface under static conditions that successfully expressed the experimental results.[32] The purpose and application of a convection flow to a small-sized space were demonstrated in a two-dimensional model of microfluidic devices.[28,29] Escobedo et al. compared the flow-through and flow-over models for the adsorption of an analyte in detail.[33] Meanwhile, due to the complexity of applying model calculations to flow-through biosensors, there are few reports on the modeling of multistep recognition (e.g., sandwich-type detection).

The aim of this study is to explain the purpose and function of our membrane-based biosensing system using a numerical approach. The numerical model considers biomolecule mass transfer, association/dissociation, and enzymatic reaction based on the experimental parameters (Figure 1b). The conventional ELISA is modeled as a comparison to demonstrate the superiority of the membrane-based system based on calculations. Moreover, the effect of each parameter of our proposed system was evaluated to obtain the systematic design which meets the sensitivity requirements of POCT.

EXPERIMENTAL SECTION

Structure of the Membrane-Based Sensor. In the membrane-based sensor, the capture antibody is covalently immobilized onto the membrane surface. A detailed description of the sensor fabrication and experimental data used in this study can be found in a previous report.[16] In brief, a track-etched polyethylene terephthalate (PET) membrane with uniform cylindrical pores (porosity 19.6%, maximum pore diameter 1 μm, and thickness 22 μm) was modified with poly(acrylic acid) by plasma graft polymerization.[17] After converting the carboxy group of the grafted polymer into the active ester group, the capture antibody was immobilized into the pores by immersing the PET membrane in the capture antibody solution (100 μL, 100 μg/mL) at 4 °C overnight (Figure 2b).

Modeling of the Proposed Membrane-Based Biosensor. Our sensor uses track-etched membranes with a pore size of 1 μm, which means that the pores have a uniform cylindrical structure. Therefore, the model is constructed through mass transfer into a 1 μm diameter tube. Biomolecules and a substrate (Ag, Ab_2, and Sub) permeate the pore and reach the reaction site near the pore surface (Figure 2).

https://doi.org/10.1021/acs.analchem.1c00250
Anal. Chem. 2021, 93, 7210−7219

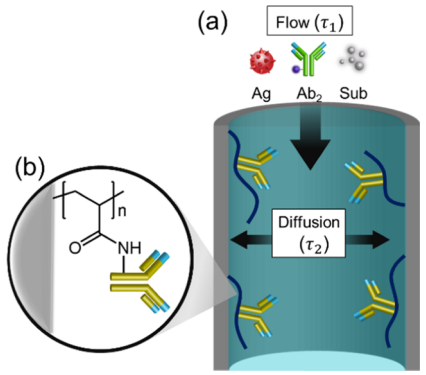

Figure 2. (a) Schematic illustration of mass transfer via solution flow and reaction in the pores. As τ_2 is much larger than τ_1, the model assumes that there is no concentration distribution in the radial direction. (b) Structure of the sensor surface.

However, because the time constant for flow (τ_1) is much larger than that for radial diffusion in the pore (τ_2), the radial diffusion rate is much faster than the flow rate in the thickness direction (see the Supporting Information). Thus, the concentration of the solution is assumed to be identical in the radial direction. Furthermore, the model was constructed considering only the solution flow because the captured biomolecules through convection flow are much larger than that by diffusion (Figure 4a in the later description).

We adopted a sandwich-type reaction system, which involves three components for sensing: flow of (1) Ag, (2) Ab_2, and (3) Sub, as shown in Figure 1b. In this study, the model is investigated with and without convection flow to determine its effect. Lax–Wendroff theorem,[34] which is a nonlinear equation with second-order accuracy in both space and time, was applied for the advective term in the model with convection flow. Meanwhile, in the model without convection flow, the region where only molecular diffusion occurs (1 mm in front of the pore inlet) was included because biomolecules are quickly consumed near the membrane inlet so that concentration gradients are formed.

In the first step, when an analyte permeates the pore, the Ag reacts with capture antibody (Ab_1), which is immobilized in the pore. This step is described as follows.

$$\text{Membrane}-Ab_1 + Ag \underset{k_{off}}{\overset{k_{on}}{\rightleftarrows}} Ab_1 - Ag \quad (1)$$

Here, k_{on} is the association rate constant and k_{off} is the dissociation rate constant.

In the second step, $Ag-Ab_1$ forms a sandwich structure with the detection antibody. Thus,

$$Ab_1 - Ag + Ab_2 \underset{k_{off}}{\overset{k_{on}}{\rightleftarrows}} Ab_1 - Ag - Ab_2 \quad (2)$$

Here, the kinetic constants are assumed to be the same as those in the first step. In addition, the dissociation/reassociation of the captured Ag, which is represented by the inverse reaction of eq 1, was also considered.

In the third step, the substrate is oxidized through horseradish peroxidase (HRP) in a sandwich structure, as follows.[35]

$$Sub \xrightarrow{k_{cat}} Sub_{ox} \quad (3)$$

Here, Sub is the substrate, Sub_{ox} is the oxidized substrate, and k_{cat} is the turnover number.

We experimentally used bovine serum albumin (BSA) as the Ag, anti-BSA polyclonal antibody as the Ab_1, HRP-labeled anti-BSA polyclonal antibody as the Ab_2, and 3,3′,5,5′-tetramethylbenzidine (TMB) as the substrate.[16] Therefore, the parameters used in this model were in accordance with these conditions.

Table 2 shows the parameters that were used in the model calculation. The parameters, φ, r_{pore}, and d_{Ab_1} were used to calculate the concentration of the immobilized Ab_1 in the pore (C_{Ab_1}). The kinetic parameters k_{on} and k_{off} were determined

Table 2. Parameters Used in the Numerical Model[16,35,37−40]

classification	parameter	symbol	unit	experimental value	refs
membrane structure	membrane thickness	l	μm	22	16
	membrane area	A	cm^2	0.785	16
	porosity	φ		19.6	16
	pore radius	r_{pore}	μm	0.5	16
	Ab_1 density per membrane area	d_{Ab_1}	ng cm^{-2}	8000	16
molecular property	association rate constant	K_{on}	m^3 mol^{-1} s^{-1}	63.5	
	dissociation rate constant	K_{off}	s^{-1}	3.7×10^{-4}	
	turnover number of TMB–HRP	k_{cat}	s^{-1}	1.3×10^{4}	37
	Michaelis constant of TMB–HRP	K_m	mM	0.415	37
	absorption coefficient of TMB_2	ε	M^{-1} cm^{-1}	3.9×10^{4}	35
	diffusion coefficient of Ag (BSA)	D_{Ag}		6×10^{-11}	38
	diffusion coefficient of Ab	D_{Ab_1}	m^2 s^{-1}	4×10^{-11}	39
	diffusion coefficient of TMB	D_{TMB}		3×10^{-10}	40
operational condition	permeated Ag concentration	C_{Ag}	M	3×10^{-11}–1.5×10^{-9}	16
	permeated Ab_2 concentration	C_{Ab_2}	M	1.3×10^{-10}	16
	permeation time	t	min	10	16
	flow rate	u	μL min^{-1}	50	16

https://doi.org/10.1021/acs.analchem.1c00250
Anal. Chem. 2021, 93, 7210−7219

experimentally by using a biolayer interferometry Octet K2 (Pall Fortebio), as shown in Figure S1. Since the polyclonal antibodies used in the experiments have multiple epitopes, the binding constants have a normal distribution, and the determined constants are their average values.[36] The experimental values are based on our previous report[16] as well as other studies on molecular properties.[35,37−39] In addition, we changed several parameters of the molecular properties (k_{on}, D_{Ag}) and all of the operational conditions (C_{Ag}, C_{Ab_2}, t, and u) in the model calculation.

Modeling of Conventional ELISA. The expected performance of ELISA was also calculated so that it could be compared with the membrane-based sensor. In ELISA, mass transfer occurs only by diffusion, and molecular recognition occurs at the surface of the well plate. In this study, COMSOL Multiphysics was used to simulate biomolecule diffusion and calculate the amount of sandwich structure that formed at the surface of the well plate. Then, the reaction-diffusion equation was solved to calculate the signal strength based on the estimated amount of sandwich formation (see the Supporting Information).

RESULTS AND DISCUSSION

Validity of the Models and Comparison of the Sensing Systems. Figure 3a,b shows a comparison of the experimental results with the calculated results of the model under the same conditions. The experimental results for ELISA are from the Bethyl Laboratories ELISA datasheet. The experimental result for the membrane-based biosensor was derived from the combined results of the BSA detection test and the detection test with contaminant human serum albumin.[16] Figure 3a,b shows that the signals for the model and experiment are similar in both the membrane-based sensor and ELISA without any fitting parameter. Although each experimental signal in our sensor is slightly higher than the calculation values, this may be due to the experimental factor, including remaining contact between the permeated solution and the membrane before the signal is emitted.

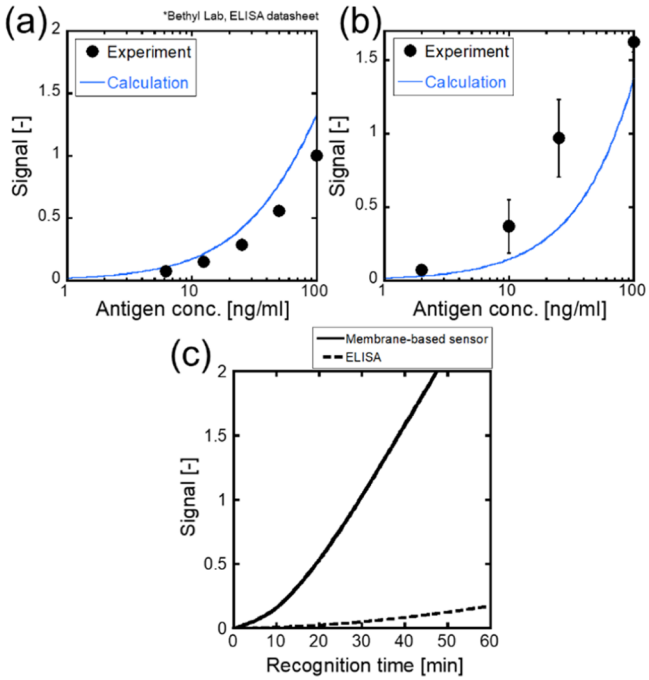

Figure 3. Comparison of the experimental signals and calculated signals via our model in the (a) ELISA and (b) membrane-based sensor. (c) Comparison between the membrane-based sensor and ELISA with the same recognition time.

Because the recognition times of the ELISA and membrane-based sensors were set to 1 h (total 2 h 30 min) and 10 min (total 35 min) in Figure 3a,b, respectively, we then calculated the effect of the reaction time to compare the sensor's performance using the same recognition time. Under these conditions, the membrane-based sensor showed a much higher signal than that of ELISA due to the efficiency of the reaction in the pore, as shown in Figure 3c. In the next section, the membrane-based sensing model is discussed in detail for each step to further explain our system.

Investigation of the First Step (Ag Recognition). To investigate the molecular-recognition behavior of the first step of the sensing system, we calculated the distribution of the captured Ag relative to the membrane thickness direction when the C_{Ag} = 10 ng/mL Ag (BSA) solution permeated the membrane under the experimental conditions, as previously reported.[16] The red line in Figure 4a shows that most of the Ags were quickly captured at the entrance of the pore; therefore, the amount of captured Ags at the exit was almost zero. In fact, according to our calculation of the total amount of accumulated Ags, most of the permeated Ags (>97%) were captured in the pore. The high reactivity was attributed to the extremely high concentration of Ab_1 in the pore.

On the other hand, as can be seen from the blue line in Figure 4a, recognition through diffusion indicated that almost no capture occurred, which was caused by the concentration gradients resulting from the consumption of the Ags around the entrance of the membrane (Figure S2). Furthermore, this tendency was observed not only for the flow of large-sized and low-diffusive biomolecules, such as the targets in this study (BSA and IgG), but also for that of small-sized and high-diffusive molecules. Figure 4b shows the amount of captured Ags relative to the channel direction when Ags of several diffusivities diffused into the pore. The result for BSA is also shown in Figure 4b ($D = 6 \times 10^{-11}$ m^2 s^{-1}, which is the same as the blue line in Figure 4a). This shows that the number of captured Ags in diffusion was low compared to that in solution flow, although small molecules (with high diffusion coefficients) enhance the influx of the Ag into the pores. Figure 4a,b shows the results for C_{Ag} = 10 ng/mL; these trends were similar regardless of the Ag concentration.

Figure 4c shows the results for solution flow when the flow rate was changed from that shown in Figure 4a. In this calculation, only the flow rate was increased at a constant recognition time, so the total amount of the permeated solution (= flow rate × recognition time) also increased. Therefore, the capture rate should also increase with the increase in flow rate. When the flow rate is low, the mass transfer is the rate-limiting step; thus, the Ag is immediately captured after reaching the pore. Meanwhile, as the flow rate increases, the breakthrough region appears and some of the Ag permeates without a reaction. Figure 4d shows the total Ags captured in the membrane at different flow rates. In a range up to 100 μl/mL (investigated in this study), the unreacted Ag is at most 10% of the total permeated amount; thus, the effect of the breakthrough is small. Although the Ag capture rate is high in this step, almost all Ab_1 remained unreacted because the initial Ab_1 concentration in the pore was much higher. Figure

https://doi.org/10.1021/acs.analchem.1c00250
Anal. Chem. 2021, 93, 7210−7219

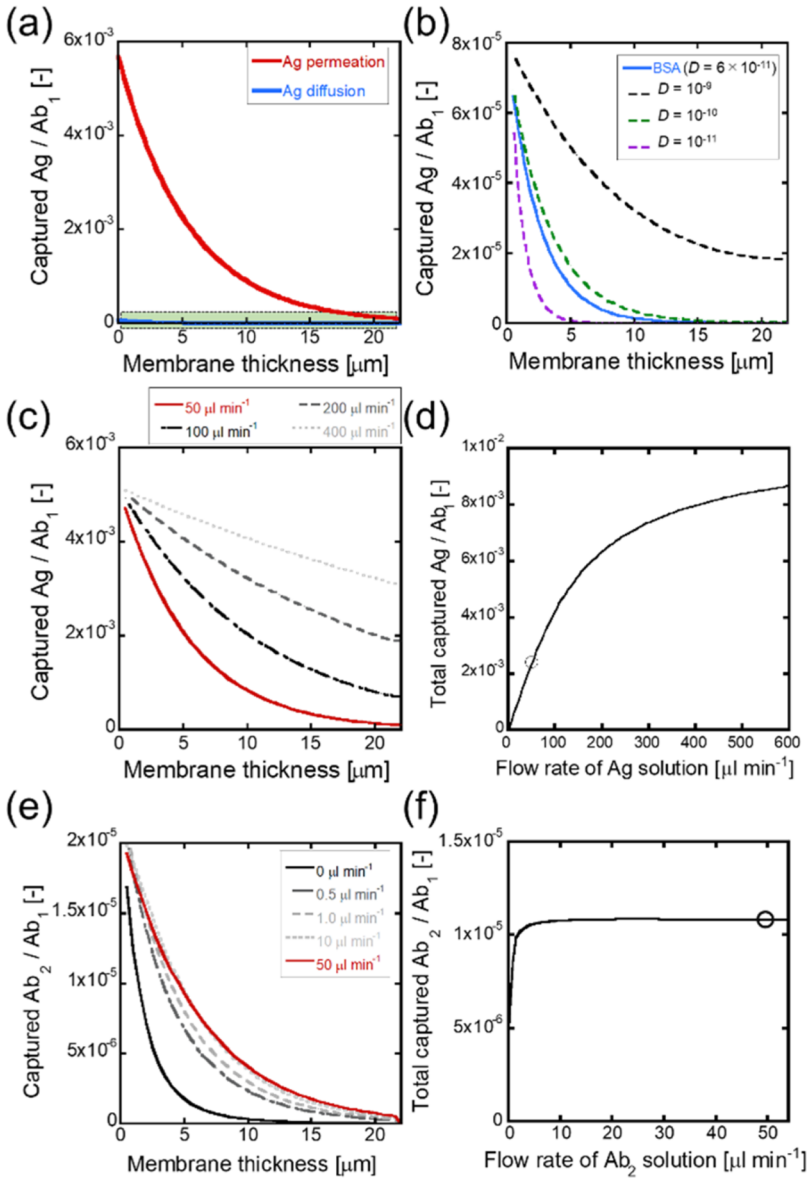

Figure 4. Amount of (a) captured Ag (BSA) via solution flow and diffusion under experimental conditions and (b) captured Ag with different diffusivities in the thickness direction. These are the results obtained with 10 ng/mL Ag concentration. The blue line in the green square in (a) is magnified in (b). (c) Distribution of captured Ag in the thickness direction with different flow rates. The Ag concentration is the same as in (a), and the other conditions are the same as the experimental conditions. (d) Total amount of captured Ag in the membrane with different flow rates. The breakthrough occurred by increasing the flow rate of the Ag solution. The plot shows the experimental condition, where a breakthrough did not occur. (e) Distribution of captured Ab_2 in the thickness direction with different flow rates. The Ag concentration in the first step is the same as in (a), and the other conditions are the same as in the experimental conditions. (f) Total amount of captured Ab_2 in the membrane with different flow rates. The plot shows the experimental conditions. Because of the low reaction rate, the total captured Ab_2 amount becomes constant with a subtle flow rate.

S3 shows the density of unreacted Ab_1 relative to the thickness direction when the Ag permeated under the same conditions as shown in Figure 4a. This result indicates that the amount of Ab_1 is enough for the Ag to recognize.

Investigation of the Second Step (Sandwich Formation). Next, we evaluated the formation of the sandwich structure in the second step of the sensing system. The red line in Figure 4e shows the amount of captured Ab_2 (i.e., sandwich structure formation) under experimental conditions when 10 ng/mL of Ag permeates in the first step; hence, the Ag distribution shown in Figure 4a is used in this calculation. As the amount of captured Ag at the entrance of the pore is high in the first step, that of Ab_2 in the second step is correspondingly high. Meanwhile, the total sandwich formation ratio was extremely low. The total amount of Ab_2 captured in the experimental condition was calculated to be <0.5% of the total amount of permeated Ab_2 (≈amount of captured Ag in the first step). This suggests that the reaction ratio of the second step can be improved, which would contribute to a direct increase in sensor sensitivity.

Figure 4e shows the results when only the flow rate in the second step was changed, while the other experimental conditions remained the same. Based on the results in Figure 4e, the total amount of Ab_2 captured in the membrane with a different flow rate is calculated as shown in Figure 4f. Unlike in the case of Figure 4d, the captured Ab_2 amount becomes

https://doi.org/10.1021/acs.analchem.1c00250
Anal. Chem. 2021, 93, 7210−7219

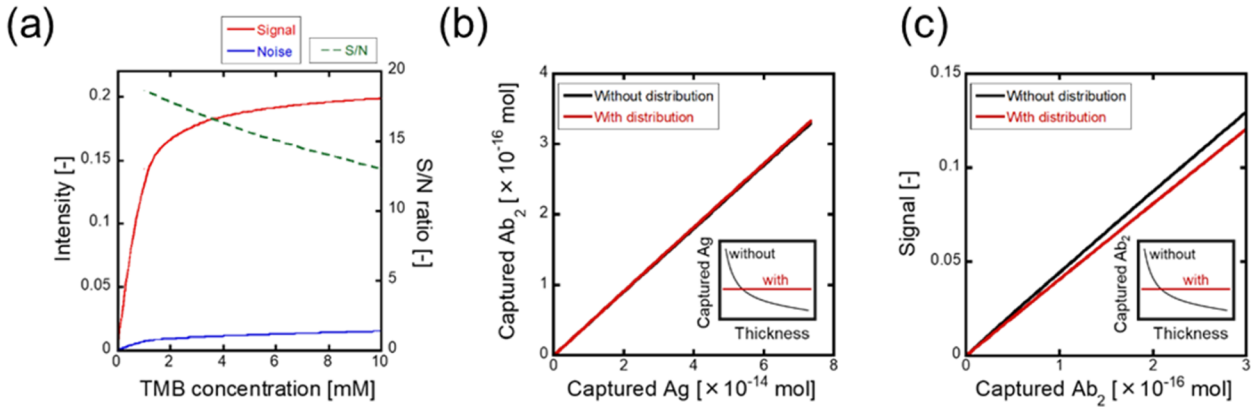

Figure 5. (a) Relationship between the signal and the noise with different TMB concentrations. The change in the S/N ratio is also included. Nonspecific binding of Ab_2 was assumed to be 5% of the specific binding, and the others were adapted to the experimental conditions. (b) Effect of the presence or absence of the distribution of the captured Ag on the amount of captured Ab_2 in the second step. The red line shows the result when 10 ng/mL Ag permeated at 0−50 μL/mL for 10 min in the first step and the Ab_2 permeated under the experimental conditions in the second step. In the black line, the distribution of Ag captured in the first step was assumed to be uniform, under the experimental conditions used in the second step. (c) Effect of the presence or absence of distribution of captured Ab_2 in the second step on the signal. The third step was assumed to be the same as the experimental conditions. The red line is the result, with the distribution shown by "with distribution" in (b), while the black line indicates uniform Ab_2 distribution. The inset of each figure shows an illustration of the assumed biomolecule distributions.

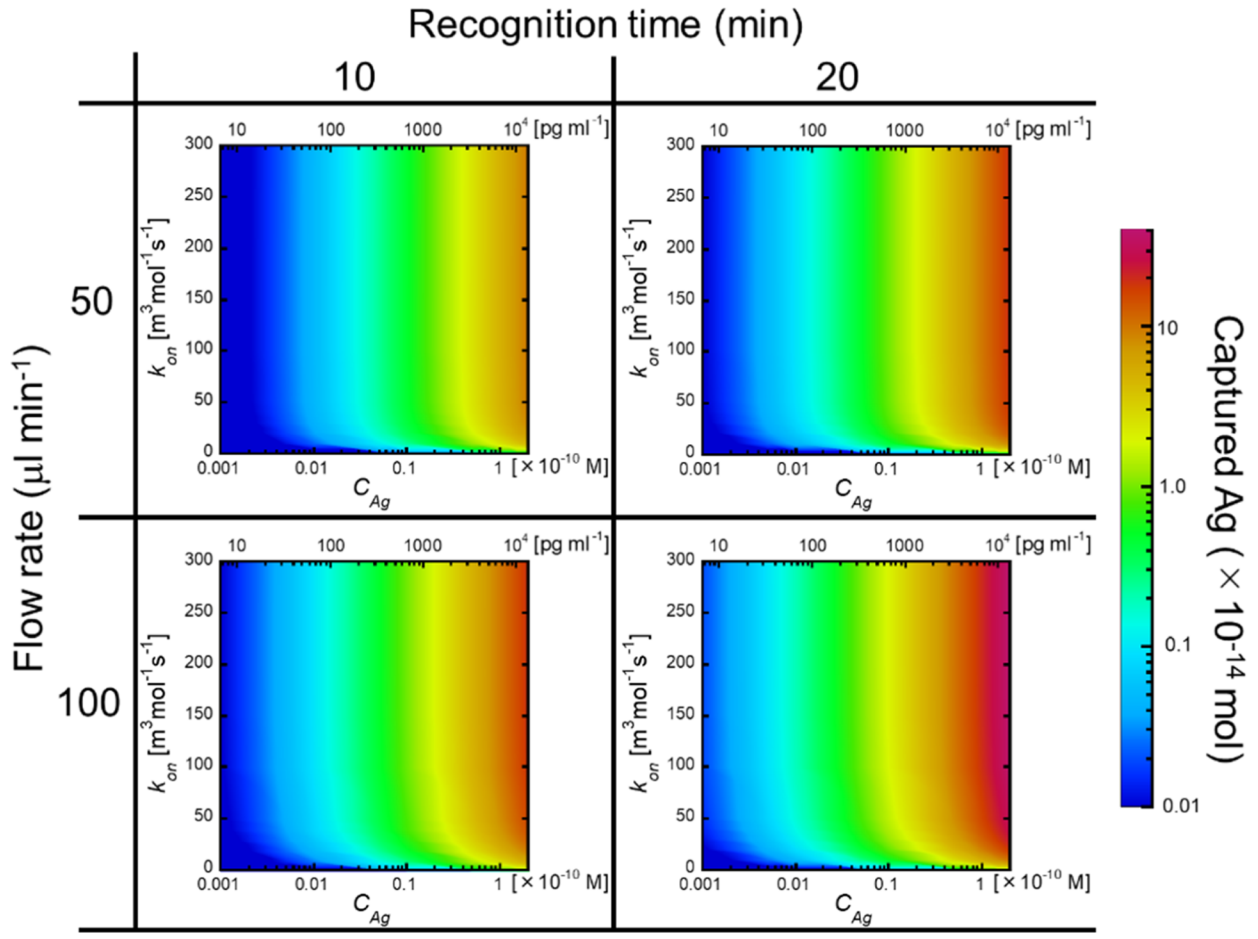

Figure 6. Mapping of the amount of captured Ag at various C_{Ag} and k_{on} in the first step. This figure includes the four types of mappings for different recognition times and flow rates.

almost constant from the low flow rate. This indicates that this step is almost independent of the flow rate and is the reaction rate-controlled process, that is, the captured amount cannot be improved by the flow rate but can be controlled by increasing the reaction time and Ab_2 concentration. This is because the Ab_1−Ag concentration in the pore is lower than the initial Ab_1 concentration, which leads to low reaction kinetics. The results also show that the flow rate of the permeated Ab_2 solution (i.e., volume of the secondary antibody solution) can be reduced while requiring a high concentration of the secondary antibody

https://doi.org/10.1021/acs.analchem.1c00250
Anal. Chem. 2021, 93, 7210−7219

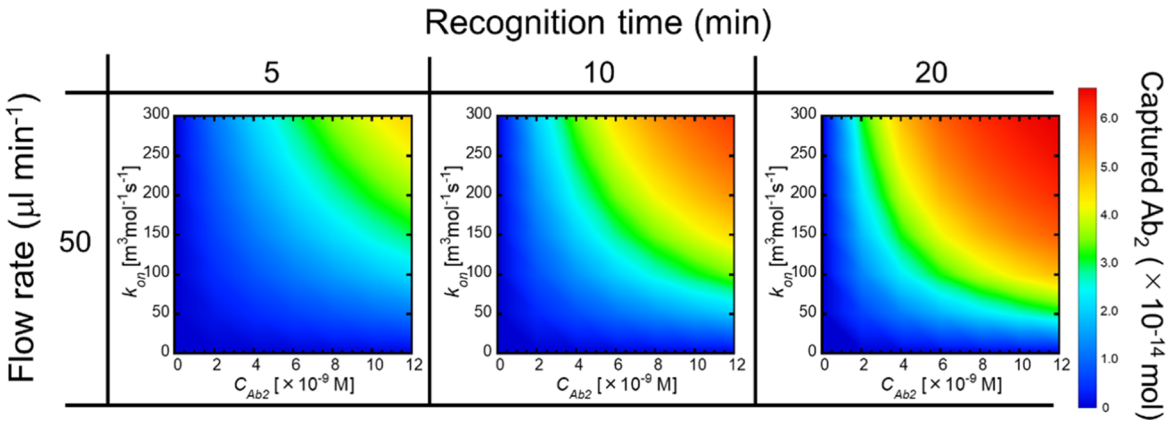

Figure 7. Color mapping of the amount of captured Ag at varying permeated Ag concentrations and k_{on}. Due to the reaction-rate-limiting observed in this step, only recognition time is considered with the conditions of C_{Ag} = 10 ng/mL and 50 μL/min for 10 min in the first step.

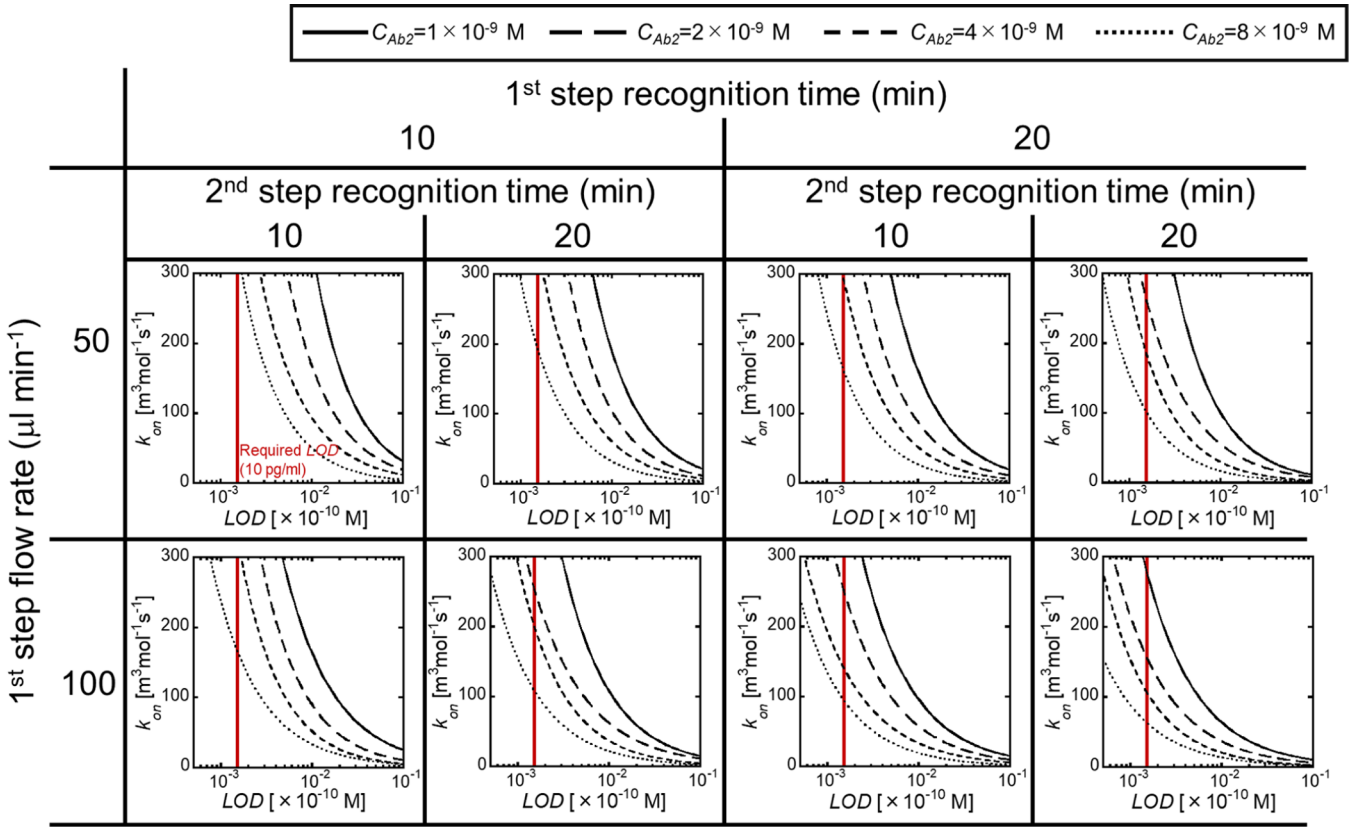

Figure 8. Calculated LOD by changing both conditions (flow rate and recognition time) in the first and second steps. The red line shows the required LOD for disease sensing.

toward achieving excellent performance. Therefore, the overall costs can be minimized by choosing both the appropriate volume and concentration of the solution. It is also effective to improve the secondary antibody structure itself (see the last section).

Investigation of the Third Step (Enzyme Reaction). In the enzymatic reaction in the third step, TMB reacts with HRP, which results in coloration. This step is based on the Michaelis−Menten equation, and the amount of TMB_2 increases as the substrate concentration, enzyme concentration, or reaction time increases. However, as the background signal also increases as the substrate concentration and reaction time increase, the signal and noise (S/N) ratio does not improve. Figure 5a shows the calculated intensity and S/N ratio using different TMB concentrations. Here all but the third step are set to the experimental conditions. Nonspecific binding of Ab_2, which results in noise, was assumed to be 5% of the specific binding. This shows that increasing the TMB concentration does not improve the S/N ratio (thus, the sensitivity was not improved). Therefore, the enzyme concentration in the pore (i.e., the amount of sandwich) needs to be increased to improve the sensitivity. The above results show that the second step needs improvement for increasing the Ab_2 capture ratio to achieve higher sensitivity of the device.

https://doi.org/10.1021/acs.analchem.1c00250
Anal. Chem. 2021, 93, 7210−7219

In addition, the distribution in the pore also changed depending on the flow conditions; however, the effect of the distribution on the signal was small. Figure 5b,c shows the amount of Ab_2 captured in the second step and the resultant signals, respectively, depending on the amount of captured Ags with or without the distribution. The red line shows the results with the Ag−Ab_1 distribution when 10 ng/mL Ag permeated at 0−50 μL/mL for 10 min, while the black line shows the calculated result without distribution of the captured Ag, where the average concentration of Ag−Ab_1 was used. The second step was calculated under experimental conditions. In both figures, it can be seen that the effect of the distribution is small and highly dependent on the number of captured biomolecules.

Design of the High-Sensitivity Detection System. In our detection system using solution flow into the pore, the following four parameters should be considered: concentration of the permeated biomolecule, flow rate, recognition time, and the kinetic parameter between the receptor and the target. The diffusion coefficient, D, is not considered because its contribution is small (Figure 4a), while ELISA is significantly affected by D. Regarding the kinetic parameter, k_{off} is ignored and only k_{on} is considered. This is because the inverse reaction is not significantly affected, even under those conditions; therefore, this should be considered when the k_{off} is larger (Figure S4).

Because the permeated Ag concentration directly affects the amount of formed sandwich structure and, thus, the LOD, the first step is first investigated as follows. Figure 6 shows the color mapping of captured Ags with different Ag concentrations and k_{on}. Here, different recognition times (10 and 20 min) and flow rates (50 and 100 μL/min) are also considered. In each condition, the amount of captured Ags increases depending on the C_{Ag}, even at low C_{Ag}, because almost all Ags are captured in these conditions, as mentioned above. These captured Ags are expected to be detected with improvements in the later steps. In addition, since the captured Ag amount in this step strongly depends on the total amount of permeated Ags (i.e., flow rate × recognition time) when no breakthrough occurs, the results in the case of 50 μL/min for 20 min and 100 μL/min for 10 min are similar. For the same reason, the captured amount in the case of 100 μL/min for 20 min is large, which suggests that even lower concentrations of Ags can be detected when a larger sample volume is available. In addition, if the k_{on} value is not small, the Ag transfer is rate-limiting, and the captured Ag amount is proportional to C_{Ag} regardless of k_{on}.

In the second step, the flow rate was not considered because the reaction is rate-limiting, as shown in the discussion in Figure 4f. Therefore, in mapping the second step (Figure 7), only the molecular-recognition time is considered with the constant flow rate. In Figure 7, the captured amount of Ab_2 improved with the recognition time. However, the effect of the recognition time is small in the red-colored region because more than 80% of the captured Ag already formed a sandwich structure. In addition, the captured Ab_2 strongly depends on both k_{on} and C_{Ag} since this step is reaction-rate-limited.

Figure 8 shows the detection limits obtained for varying conditions in both the first and second steps, which were obtained by combining the calculations in Figures 6 and 7. The LOD is calculated using the following equation.[41]

$$\mathrm{LOD} = 3.3\, s/a \tag{4}$$

Here, s is the standard deviation of absorbance at an Ag concentration of 0 ng/mL and a is the calibration slope around the detection limit.

The red line in Figure 8 shows the required sensitivity (10 pg/mL), which is determined from cut-off values of biomarkers such as interleukin and tumor necrosis factor.[42] The results shown in Figure 8 were affected by both Figures 6 and 7. As shown in Figure 6, the results are similar for the cases of 50 μL/min for 20 min and 100 μL/min for 10 min, while the case of 100 μL/min for 20 min has the lowest detection limit. Furthermore, reflecting the results in Figure 7, a longer recognition time of the Ab_2 can lower the detection limit. This result also suggests that it is possible to detect the Ag with pg/mL sensitivity by selecting the appropriate Ag−Ab system and experimental conditions.

One of the improved calibration curves (using condition 1:500 μL of the analyte, $C_{Ab_2} = 1.2 \times 10^{-8}$ M, 50 μL/min for 10 min in the first step and 50 μL/min for 20 min in the second step) is shown in Figure 9. The calculated results

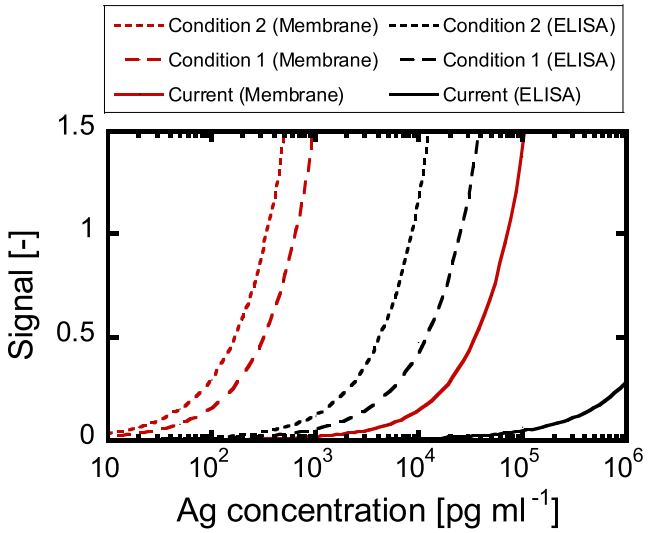

Figure 9. Comparison of the calibration curves of the membrane-based system and ELISA with improved and current conditions. In condition 1, the operational parameters were improved ($C_{Ab2} = 1.2 \times 10^{-8}$ M, 40 min recognition time: 10 min for the first step and 20 min for the second step. The flow rate for the membrane-based system is 50 μL/min, which is the same as the current condition). In condition 2, the kinetic parameter is changed to $k_{on} = 300$ m^3 mol^{-1} s^{-1}.

suggest that the LOD could be lowered by 2 orders of magnitude by improving operational conditions. The improved membrane-based system has more than 10 times higher sensitivity than ELISA under the same improved conditions. Curves with an improved kinetic parameter ($k_{on} = 300$ m^3 mol^{-1} s^{-1}) are also shown. In this condition (condition 2), the sandwich formation is more than 90%; thus, the maximum performance is around this curve. Meanwhile, detection at even lower concentrations is possible if a larger analyte volume is available, as discussed above. In addition, increasing the concentration of enzymes by designing an Ab_2 complex structure can improve sensitivity while reducing the amount of antibody.[2] By combining the application of such receptors with our strategies for improving the sandwich formation ratio, we expect to achieve even higher sensitivity with the membrane-based sensor. The experimental improvements

https://doi.org/10.1021/acs.analchem.1c00250
Anal. Chem. 2021, 93, 7210−7219

based on the proposed design concept are under investigation, and the results will be reported in the near future.

In summary, we modeled our membrane-based biosensor by considering the mass transfer and biomolecular recognition with convection flow in the membrane pore. The conventional ELISA method is also modeled as a comparison. Both models reproduced the experimental results and confirmed the superiority of the membrane-based sensor over the ELISA. For the membrane-based sensor, correlations between the amount of captured biomolecules and various parameters (flow rate, recognition time, diffusion coefficient, and kinetic parameters) were investigated at each step. In the first step, it was found that the membrane-based sensor captures almost all Ags during the solution flow. This high reactivity is triggered by the high Ag_1 density in the pores. Meanwhile, in the second step, the effect of solution flow is small, and the formation rate of the sandwich structure is low in conventional conditions. In this study, we found that the use of appropriate receptors and an increase in the concentration of Ab_2 solved this problem and improved the sensitivity to the pg/mL order, which is required for POCT. This study provides guidance for designing a rapid, easy-to-use, and sensitive sensor, and it is one of the few reports that incorporate numeric modeling into the sensor design, which is expected to be helpful for future sensor development.

■ ASSOCIATED CONTENT

Supporting Information

The Supporting Information is available free of charge at https://pubs.acs.org/doi/10.1021/acs.analchem.1c00250.

Experimental details; modeling of the detection systems; materials used and fabrication of the membrane-based immunosensor; buffer flow test and calculation of pore diameter, quantification of antibody density inside the pores, biolayer interferometry data to derive k_{on} and k_{off} values; and schematic image of the model without flow (PDF)

■ AUTHOR INFORMATION

Corresponding Author

Takeo Yamaguchi − *Laboratory for Chemistry and Life Science, Institute of Innovative Research, Tokyo Institute of Technology, Yokohama, Kanagawa 226-8503, Japan;* orcid.org/0000-0001-9043-4408; Email: yamag@res.titech.ac.jp

Authors

Hiroto Okuyama − *Laboratory for Chemistry and Life Science, Institute of Innovative Research, Tokyo Institute of Technology, Yokohama, Kanagawa 226-8503, Japan;* orcid.org/0000-0003-2964-964X

Takanori Tamaki − *Laboratory for Chemistry and Life Science, Institute of Innovative Research, Tokyo Institute of Technology, Yokohama, Kanagawa 226-8503, Japan;* orcid.org/0000-0002-7728-9397

Yuhei Oshiba − *Laboratory for Chemistry and Life Science, Institute of Innovative Research, Tokyo Institute of Technology, Yokohama, Kanagawa 226-8503, Japan;* orcid.org/0000-0002-6029-3293

Hiroshi Ueda − *Laboratory for Chemistry and Life Science, Institute of Innovative Research, Tokyo Institute of Technology, Yokohama, Kanagawa 226-8503, Japan;* orcid.org/0000-0001-8849-4217

Complete contact information is available at: https://pubs.acs.org/10.1021/acs.analchem.1c00250

Notes

The authors declare no competing financial interest.

■ ACKNOWLEDGMENTS

We thank Akihito Inoue for helping with the biological analysis.

■ REFERENCES

(1) Britz, D.; Baronas, R.; Gaidamauskaitė, E.; Ivanauskas, F. *Nonlinear Anal. Model Contr.* **2009**, *14*, 419−433.
(2) Liu, D.; Huang, X.; Wang, Z.; Jin, A.; Sun, X.; Zhu, L.; Wang, F.; Ma, Y.; Niu, G.; Hight Walker, A. R.; Chen, X. *ACS Nano* **2013**, *7*, 5568−5576.
(3) Pauli, G. E. N.; De La Escosura-Muniz, A.; Parolo, C.; Bechtold, I. H.; Merkoci, A. *Lab Chip* **2015**, *15*, 399−405.
(4) Zhang, P.; Bao, Y.; Draz, M.; Lu, H.; Liu, C.; Han, H. *Int. J. Nanomed.* **2015**, *10*, 6161−6173.
(5) Horak, J.; Dincer, C.; Qelibari, E.; Bakirci, H.; Urban, G. *Sens. Actuators, B* **2015**, *209*, 478−485.
(6) Chen, P.; Chung, M. T.; McHugh, W.; Nidetz, R.; Li, Y.; Fu, J.; Cornell, T. T.; Shanley, T. P.; Kurabayashi, K. *ACS Nano* **2015**, *9*, 4173−4181.
(7) Gold, L.; Ayers, D.; Bertino, J.; Bock, C.; Bock, A.; Brody, E. N.; Carter, J.; Dalby, A. B.; Eaton, B. E.; Fitzwater, T.; Flather, D.; Forbes, A.; Foreman, T.; Fowler, C.; Gawande, B.; Goss, M.; Gunn, M.; Gupta, S.; Halladay, D.; Heil, J.; et al. *PLoS One* **2010**, *5*, No. e15004.
(8) Berezovski, M. V.; Lechmann, M.; Musheev, M. U.; Mak, T. W.; Krylov, S. N. *J. Am. Chem. Soc.* **2008**, *130*, 9137−9143.
(9) Kimoto, M.; Yamashige, R.; Matsunaga, K.-i.; Yokoyama, S.; Hirao, I. *Nat. Biotechnol.* **2013**, *31*, 453−457.
(10) Ellington, A. D.; Szostak, J. W. *Nature* **1990**, *346*, 818−822.
(11) Darwish, N. T.; Alias, Y. B.; Khor, S. M. *Trac. Trends Anal. Chem.* **2015**, *67*, 45−55.
(12) Sano, T.; Smith, C.; Cantor, C. *Science* **1992**, *258*, 120−122.
(13) Gan, S. D.; Patel, K. R. *J. Invest. Dermatol.* **2013**, *133*, No. e12.
(14) Liu, X.; Dai, Q.; Austin, L.; Coutts, J.; Knowles, G.; Zou, J.; Chen, H.; Huo, Q. *J. Am. Chem. Soc.* **2008**, *130*, 2780−2782.
(15) Bai, Y.; Koh, C. G.; Boreman, M.; Juang, Y.-J.; Tang, I.-C.; Lee, L. J.; Yang, S.-T. *Langmuir* **2006**, *22*, 9458−9467.
(16) Okuyama, H.; Oshiba, Y.; Yamaguchi, T. *Anal. Chem.* **2019**, *91*, 14178−14182.
(17) Yamaguchi, T.; Nakao, S.; Kimura, S. *Macromolecules* **1991**, *24*, 5522−5527.
(18) Kuroki, H.; Ohashi, H.; Ito, T.; Tamaki, T.; Yamaguchi, T. *J. Membr. Sci.* **2010**, *352*, 22−31.
(19) Chi, X.; Ohashi, H.; Yamaguchi, T. *Plasma Process. Polym.* **2014**, *11*, 306−314.
(20) Okuyama, H.; Oshiba, Y.; Ohashi, H.; Yamaguchi, T. *Small* **2018**, *14*, 1870082.
(21) Cheng, C.-M.; Martinez, A. W.; Gong, J.; Mace, C. R.; Phillips, S. T.; Carrilho, E.; Mirica, K. A.; Whitesides, G. M. *Angew. Chem. Int. Ed.* **2010**, *49*, 4771−4774.
(22) von Lode, P. *Clin. Biochem.* **2005**, *38*, 591−606.
(23) Liu, Y.; Wang, H.; Huang, J.; Yang, J.; Liu, B.; Yang, P. *Anal. Chim. Acta* **2009**, *650*, 77−82.
(24) Eteshola, E.; Leckband, D. *Sens. Actuators, B* **2001**, *72*, 129−133.
(25) Yatsushiro, S.; Akamine, R.; Yamamura, S.; Hino, M.; Kajimoto, K.; Abe, K.; Abe, H.; Kido, J.; Tanaka, M.; Shinohara, Y.; Baba, Y.; Ooie, T.; Kataoka, M. *PLoS One* **2011**, *6*, No. e18807.
(26) Zhang, S.; Garcia-D'Angeli, A.; Brennan, J. P.; Huo, Q. *Analyst* **2014**, *139*, 439−445.

(27) Kurihara, K.; Suzuki, K. *Anal. Chem.* **2002**, *74*, 696−701.
(28) Hu, G.; Gao, Y.; Li, D. *Biosens. Bioelectron.* **2007**, *22*, 1403−1409.
(29) Zimmermann, M.; Delamarche, E.; Wolf, M.; Hunziker, P. *Biomed. Microdevices* **2005**, *7*, 99−110.
(30) Nabaei, V.; Chandrawati, R.; Heidari, H. *Biosens. Bioelectron.* **2018**, *103*, 69−86.
(31) Vijayendran, R. A.; Ligler, F. S.; Leckband, D. E. *Anal. Chem.* **1999**, *71*, 5405−5412.
(32) Alam, M. N.; Ricardez-Sandoval, L.; Pawliszyn, J. *Anal. Chem.* **2015**, *87*, 9846−9854.
(33) Escobedo, C.; Brolo, A. G.; Gordon, R.; Sinton, D. *Anal. Chem.* **2010**, *82*, 10015−10020.
(34) Himr, D. Numerical simulation of water hammer in low pressurized pipe: comparison of SimHydraulics and Lax-Wendroff method with experiment. In *Efm12—Experimental Fluid Mechanics 2012*; Dancova, P., Novonty, P., Eds.; E D P Sciences: Cedex A, 2013.
(35) Josephy, P. D.; Eling, T.; Mason, R. P. *J. Biol. Chem.* **1982**, *257*, 3669−3675.
(36) Poulsen, T. R.; Meijer, P.-J.; Jensen, A.; Nielsen, L. S.; Andersen, P. S. *J. Immunol.* **2007**, *179*, 3841−3850.
(37) Tian, Z.; Li, J.; Zhang, Z.; Gao, W.; Zhou, X.; Qu, Y. *Biomaterials* **2015**, *59*, 116−124.
(38) Raj, T.; Flygare, W. H. *Biochemistry* **1974**, *13*, 3336−3340.
(39) Yadav, S.; Sreedhara, A.; Kanai, S.; Liu, J.; Lien, S.; Lowman, H.; Kalonia, D. S.; Shire, S. J. *Pharm. Res.* **2011**, *28*, 1750−1764.
(40) Baldrich, E.; del Campo, F. J.; Muñoz, F. X. *Biosens. Bioelectron.* **2009**, *25*, 920−926.
(41) Miller, J. C. M. J. *Statistics for Analytical Chemistry*, 4th ed.; Ellis-Howood: NY, 1993; p 115.
(42) Jung, C.-C.; Liang, H. H.; Lee, H. L.; Hsu, N. Y.; Su, H. J. *PLoS One* **2014**, *9*, No. e95791.

https://doi.org/10.1021/acs.analchem.1c00250
Anal. Chem. 2021, 93, 7210−7219